Selective vulnerability of parvocellular oxytocin neurons in social dysfunction

Masafumi Tsurutani [1,2], Teppei Goto[1], Mitsue Hagihara[1], Satsuki Irie[1] & Kazunari Miyamichi [1] ✉

Selective vulnerability offers a conceptual framework for understanding neurodegenerative disorders such as Parkinson's disease, where specific neuronal types are selectively affected and adjacent ones are spared. However, the applicability of this framework to neurodevelopmental disorders, particularly those characterized by atypical social behaviors, such as autism spectrum disorder, remains uncertain. Here we show that an embryonic disturbance, known to induce social dysfunction in male mice, preferentially impaired the gene expression crucial for neural functions in parvocellular oxytocin (OT) neurons—a subtype linked to social rewards—while neighboring cell types experienced a lesser impact. Chemogenetic stimulation of OT neurons at the neonatal stage ameliorated social deficits in early adulthood, concurrent with cell-type-specific sustained recovery of pivotal gene expression within parvocellular OT neurons. Collectively, our data shed light on the transcriptomic selective vulnerability within the hypothalamic social behavioral center and provide a potential therapeutic target through specific neonatal neurostimulation.

The applicability of the selective vulnerability framework[1] to neurodevelopmental disorders (NDDs) remains uncertain. The pathogenesis of NDDs is closely associated with fetal genetic factors and maternal/environmental influences, such as maternal immune activation, gut microbiota, and medications administered during fetal brain development[2–5]. As these factors exert systemic effects on the entire nervous system, the precise mechanisms underlying the pathogenesis of NDDs remain largely elusive. For example, despite rapid advancements in our understanding of the neural circuits that regulate social behaviors in rodents[6,7], it remains unclear whether specific neural cell types are selectively affected in pathological conditions that model NDDs. To fill this knowledge gap, in this study, we focus on the OT neurons in the paraventricular hypothalamus (PVH^OT neurons) in mouse models that exhibit social dysfunction.

Decades of rodent studies have highlighted the significance of the OT system in the typical development of social behaviors, bond formation, and parental behaviors[6,8,9]. Numerous brain regions express OT receptors[10], emphasizing their widespread functions throughout the brain. Among the population of OT neurons, magnocellular PVH^OT neurons exhibit bifurcated axonal projections to the posterior pituitary and various forebrain structures[11]. By contrast, parvocellular PVH^OT neurons selectively project to the central brain, including the ventral tegmental area and substantia nigra, thereby modulating the dopamine system and contributing to social reward[12–14]. Additionally, parvocellular PVH^OT neurons innervate the hindbrain and spinal cord, exerting diverse neuromodulatory effects on emotions, appetite, and pain[11,15].

Impairment of the OT system has been extensively documented in various genetic and environmental rodent models of social dysfunction. For instance, reductions in OT immunoreactivity or *OT* mRNA expression within the PVH have been observed in genetic mutants of the *Shank3b* gene[5,16], *Maged1* gene[17], *Necdin* gene[18], the progeny of mothers consuming a high-fat diet[4], and rats prenatally exposed to valproic acid (VPA)[19,20]. However, these studies have not discerned whether the observed reduction stems from a decline in OT expression or a loss of PVH^OT neurons at the cellular level. Furthermore, the

[1]Laboratory for Comparative Connectomics, RIKEN Center for Biosystems Dynamics Research, Kobe, Hyogo, Japan. [2]Graduate School of Biostudies, Kyoto University, Kyoto, Kyoto, Japan. ✉e-mail: kazunari.miyamichi@riken.jp

potential impacts on distinct cell types of PVH[OT] neurons remain unknown. A recent seminal study employing single-cell RNA sequencing (RNA-seq) unveiled distinct transcriptomic signatures of magnocellular and parvocellular PVH[OT] neurons, with the latter displaying enriched expression of autism spectrum disorder (ASD) risk factor genes[21] and playing a more significant role in social reward[12]. This leads us to hypothesize that parvocellular PVH[OT] neurons may be more susceptible to disruptions caused by embryonic factors that induce social dysfunctions.

Result

Histochemical analyses of OT ligands in parvocellular PVH[OT] neurons

We first examined a mouse model of prenatal exposure to VPA[19,22]. In the present study, we exclusively utilized male mice, as male-biased impacts of prenatal VPA exposure on social behaviors have previously been documented[19,23]. We confirmed that VPA-treated male *OT-Cre* mice[24] on the C57BL/6 background exhibited decreased sociability, as assessed by the three-chamber test (Fig. 1a). In contrast to control mice with prenatal saline exposure, which spent significantly more time investigating a cage containing an unfamiliar mouse compared with a cage with a non-animal object, the VPA-treated group failed to show this preference (Fig. 1b). We then performed intravenous Fluoro-Gold

(FG) injection to visualize magnocellular but not parvocellular PVH[OT] neurons selectively based on the fact that only magnocellular OT neurons send axonal projections outside the blood–brain barrier[12] (Fig. 1c). Additionally, we utilized *OT-Cre; Ai9* (tdTomato Cre reporter mouse line[25]) double knockin mice to label OT neurons genetically regardless of OT ligand expression at the time of analysis. We found that the total number of tdTomato-labeled cells was unaltered in VPA-treated mice (Fig. 1d). Consistent with previous research[12], FG+ magnocellular PVH[OT] neurons were located in the anterior part of the PVH, whereas FG− putative parvocellular PVH[OT] neurons were located in the posterior part (Fig. 1e, f). The number of OT-expressing cells, as detected by anti-OT antibodies, was selectively reduced in the parvocellular PVH[OT] neurons (Fig. 1g, top). Quantitative analysis of fluorescent intensity indicated a significant reduction of OT ligand expression in both types of PVH[OT] neurons, with a more pronounced reduction in the parvocellular PVH[OT] neurons (Fig. 1g, bottom). These findings exclude the possibility of a cellular loss of PVH[OT] neurons in VPA-treated mice and demonstrate a reduction in OT expression at the protein level, preferentially affecting parvocellular PVH[OT] neurons.

To examine the generality of these findings, we conducted similar experiments in male mice born to mothers that had been fed a high-fat diet, which we refer to as the maternal high-fat diet (MHFD) group for simplicity (Supplementary Fig. 1a). Consistent with a previous study[4],
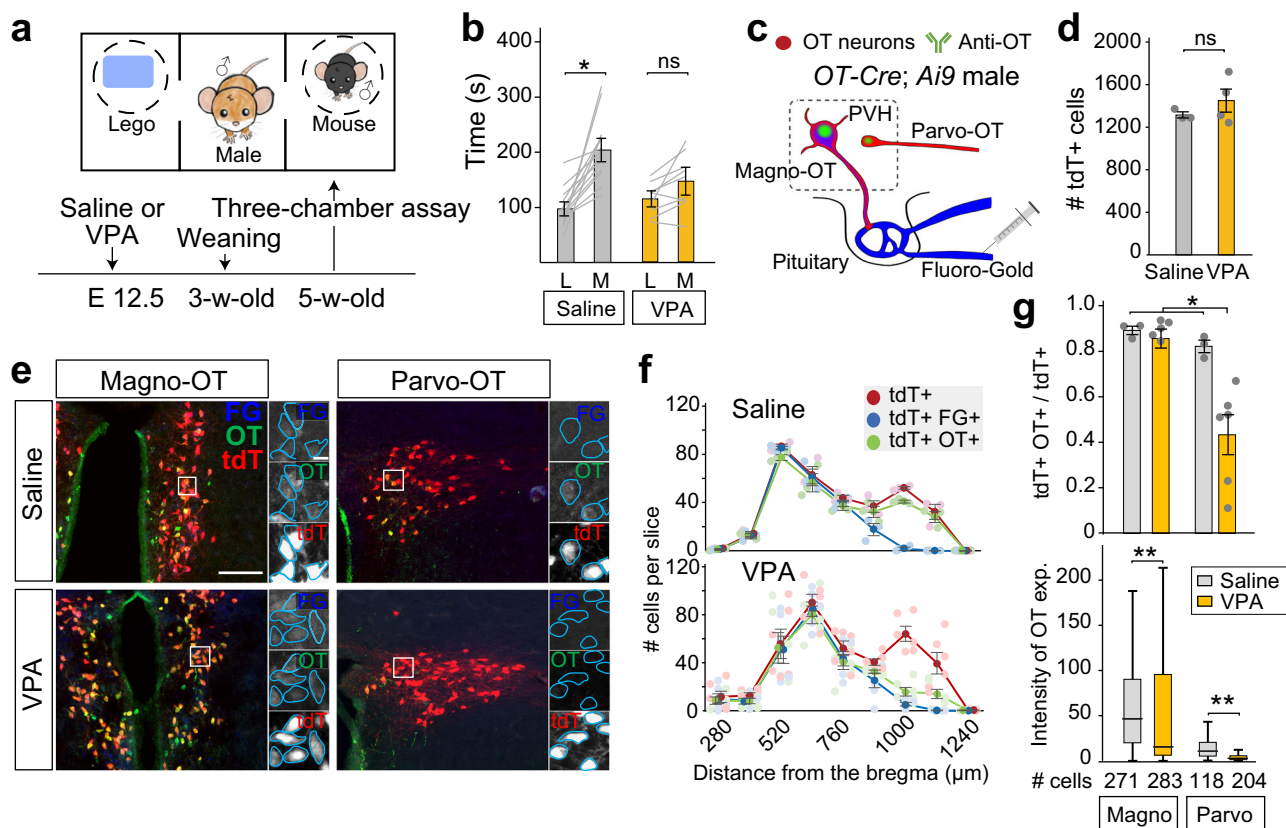
Fig. 1 | Reduction of OT ligand expression in the parvocellular PVH[OT] neurons of VPA-treated male mice. a Time line of the experiment (bottom) and schematic diagram of the three-chamber assay (top). E, embryonic day. **b** Duration of mice actively engaged in sniffing and exploring the grid containing a nonsocial object (Lego block, L) and an unfamiliar male mouse (M). $N = 14$ for the saline and $N = 9$ for the VPA group. *$p < 0.05$ by the two-sided Wilcoxon rank-sum test. **c** Schematic diagrams depicting the labeling strategy. **d** Number of tdT+ cells in the PVH. No difference was detected by the two-sided Wilcoxon rank-sum test. $N = 3$ and 4 for the saline and VPA groups. **e** Typical coronal sections of the PVH showing tdTomato (tdT +), anti-OT staining (OT+), and Fluoro-Gold (FG+). Scale bars, 200 μm for low-magnification images and 20 μm for magnified images. **f** Number of tdT+, tdT+ FG+,

and tdT+ OT+ cells per slice. $N = 3$ and 6 for the saline and VPA groups, respectively. **g** (Top) Fraction of tdT+ OT+ cells over tdT+ cells. *$p < 0.05$ by two-way ANOVA with the post-hoc Tukey–Kramer test. $N = 3$ and 6 for the saline and VPA groups. (Bottom) Fluorescent intensity of anti-OT staining. The indicated number of cells were counted, from $N = 3$ animals each for the saline and VPA groups. The horizontal line within the box denotes the median, the upper and lower sides of the box indicate the first and the third quartiles, and whiskers represent the maximum and minimum values within a distance that extends to 1.5 times the interquartile range. **$p < 0.01$ by the two-sided Wilcoxon rank-sum test with Bonferroni correction. Error bars, SEM. For more data, see Supplementary Fig. 1. See Supplementary Information for exact *p*-values. Source data are provided as Source Data files.

the MHFD group showed impaired social behaviors without a body weight phenotype (Supplementary Fig. 1b, c). We observed a significant reduction of anti-OT immunostaining along the entire anterior–posterior axis of the PVH, without affecting the total number of *Ai9*-labeled cells (Supplementary Fig. 1d–f). Focusing on the posterior part of the PVH where the parvocellular PVH[OT] neurons exist, we observed a significant decrease in the number of OT ligand-expressing cells and fluorescent intensity in individual cells in the MHFD compared with the RD control group (Supplementary Fig. 1g). These results indicate that two independent mouse models exhibiting atypical sociability because of exogenous or maternal factors commonly display reduced OT ligand expression in parvocellular PVH[OT] neurons.

Aberrant gene expression in parvocellular PVH[OT] neurons

Next, we aimed to investigate whether the reduction in OT expression occurred at the mRNA level and, if so, whether aberrant gene expression was specific to the *OT* gene or more widespread. Additionally, we aimed to assess the impact on other neural cell types located within or near the PVH. To address these inquiries, we surgically dissected a hypothalamic region containing the PVH from VPA-treated *OT-Cre; Ai9* male mice, as well as from the control group prenatally exposed to saline. Single nucleus (sn) RNA-seq profiles were obtained using the 10X Genomics Chromium platform for 10,060 cells in the VPA-treated group and 3750 cells in the saline-treated group that met quality control standards (Methods). We combined the sequencing data from both groups and employed unsupervised graph-based clustering using Cell Ranger[26] and Seurat[27] to classify 30 clusters of excitatory neurons expressing *vesicular glutamate transporter type 2* (*vGluT2*) (Fig. 2a, b), following a more general categorization (Supplementary Figs. 2 and 3). The VPA- and saline-treated groups were intermingled within these excitatory clusters, indicating that VPA did not affect the overall transcriptomic signature (Fig. 2a and Supplementary Fig. 2d).

OT-positive clusters were readily identifiable owing to their distinctive expression of *OT* genes (Fig. 2b, c). Based on an analysis of gene expression, including *Sox5*, *estrogen receptor type 2* (*Esr2*), and *Reelin* genes, as outlined in a previous study[12] and our own in situ hybridization (ISH) data (Supplementary Fig. 4), we were able to identify the parvocellular (cluster 18) and magnocellular (cluster 19) PVH[OT] neurons (Fig. 2c, d). Differentially expressed genes (DEGs) between the VPA-treated and control groups were defined as those exhibiting a >1.4-fold change and satisfying a false discovery rate criterion of <0.05 (Fig. 2e, Supplementary Fig. 3b). Notably, the expression of the *OT* gene itself was significantly reduced in the parvocellular PVH[OT] neurons of VPA-treated compared with saline-treated control mice (Fig. 2d, e), suggesting that the observed downregulation of OT ligand expression (Fig. 1e–g) is a result of decreased mRNA expression. We found varying numbers of both upregulated and downregulated DEGs among the top 25 *vGluT2*-positive (+) clusters (Fig. 2f). Additionally, we identified variable numbers of DEGs that were previously designated as high-confidence ASD risk factor genes[21] within each *vGluT2*+ cluster (Fig. 2g). Importantly, each cluster displayed a distinct set of ASD risk factor DEGs, with only a small fraction of genes common in two or more clusters (see Source Data files). For instance, the magnocellular and parvocellular PVH[OT] neurons showed completely nonoverlapping sets of ASD risk factor DEGs (Fig. 2h). These data demonstrate that VPA affects not only the *OT* gene in parvocellular PVH[OT] neurons, but also numerous other genes, including diverse ASD risk factor genes, in broad cell clusters near and within the PVH.

We then conducted Gene Ontology (GO) analysis[28,29] for the DEGs found within the top 25 *vGluT2*+ clusters (Fig. 3a). Among them, the parvocellular PVH[OT] neurons (cluster 18) exhibited the highest number of significantly associated GO terms for both upregulated and downregulated DEGs (Fig. 3a, Supplementary Fig. 5, and Source Data files). Specifically, we observed an enrichment of DEGs involved in synaptic functions, behavioral regulations, and intracellular signal transduction

in the parvocellular PVH[OT] neurons, whereas the DEGs in the arginine vasopressin (AVP; cluster 11) or magnocellular PVH[OT] (cluster 19) neurons displayed little or no association with these functions. Moreover, after subjecting the downregulated DEGs to pathway analysis[30], we found that parvocellular PVH[OT] neurons were significantly affected in the largest number of signaling pathways with diverse biological functions (Fig. 3b, Supplementary Fig. 5). These pathways involved the phosphatidylinositol 3-kinase (PI3K)/protein kinase B (Akt) signaling pathway (Fig. 3c), which is relevant to the subcellular integration of the synaptic neurotransmission and neural plasticity in the brain[31]. ASD risk factor genes were predominantly enriched in this pathway (Supplementary Fig. 5b). By contrast, pathways significantly associated with the upregulated DEGs were more enriched in other cell clusters (Supplementary Fig 5c). To validate the DEGs using an independent method, we visualized the expression of some of the downregulated ASD risk factor DEGs found in the parvocellular PVH[OT] neurons in vivo through ISH. All eight genes that we examined exhibited a significant reduction in mRNA expression (Supplementary Fig. 6). Notably, the downregulation of PI3K/Akt pathway-related genes, such as *Erbb4*, *Ntrk2*, and *Tsc1*, was confirmed. These findings suggest that parvocellular PVH[OT] neurons are not distinct based on the numbers of DEGs or ASD risk factor DEGs, but rather, distinguished by a unique impact on crucial neural functions and pathways in VPA-treated mice.

In addition to the excitatory clusters, our data also suggested a potential abnormality in gene expression profiles in the inhibitory neurons within or near the PVH. Unsupervised graph-based clustering revealed 17 clusters positive for the *glutamate decarboxylase type 2* (*GAD2*) gene (Supplementary Fig. 7a, b). We found varying numbers of both upregulated and downregulated DEGs and ASD risk factor DEGs in the *GAD2*-positive clusters (Supplementary Fig 7c, d). Among them, cluster 10 (positive for *estrogen receptor type 1* gene, or *Esr1*) and cluster 11 (positive for *thyrotropin-releasing hormone receptor* gene, or *Trhr*) showed particular enrichments of diverse GO terms, such as synaptic and sensory functions (Supplementary Fig. 7e). These neurons may also contribute to the atypical sociability observed in VPA-treated mice. However, we do not rule out the possibility that their transcriptomic alterations may be due to aberrant parvocellular PVH[OT] neurons, as previous studies have reported that OT ligands are involved in the maturation of GABAergic neurons[32].

In summary, our data suggest that the effects of embryonic VPA treatment on gene expression patterns are heterogeneous and cell-type-specific. Certain gene expression networks relevant to critical neural functions are selectively vulnerable in some specific cell types within and near the PVH, including the parvocellular PVH[OT] neurons.

Activation of PVH[OT] neurons to restore atypical social behavior

Chemogenetic activation[33] of PVH[OT] neurons has been widely employed to facilitate prosocial behaviors[16,34] and potentially ameliorate atypical sociability in rodent models, specifically in *Cntnap2*-deficient mice[35,36] and *Shank3*-deficient rats[37]. Similarly, intranasal or intraperitoneal administration of OT has demonstrated a positive impact on social behaviors in *Shank3b*-deficient mice[5], *Maged1*-deficient mice[17], inbred mouse strains (BALB/cByJ and C58/J)[38], and VPA-treated rats[20]. However, the effects of such manipulations on the aberrant gene expression of PVH[OT] neurons remain unknown. Given that intranasal or intraperitoneal OT administration may not directly activate endogenous OT neurons or central OT receptors[39], we focused on the chemogenetic activation strategy. We first used an adeno-associated virus (AAV) vector to target hM3Dq-mCherry to the PVH[OT] neurons of VPA-treated *OT-Cre* mice, with a control virus expressing only mCherry. Additionally, we prepared an hM3Dq-expressing control group that was embryonically exposed to saline (Fig. 4a). Social behaviors, as assessed using the three-chamber test at 5 weeks of age, were not affected by clozapine-N-oxide (CNO) administration in the saline-treated group (Fig. 4b). Atypical social behaviors
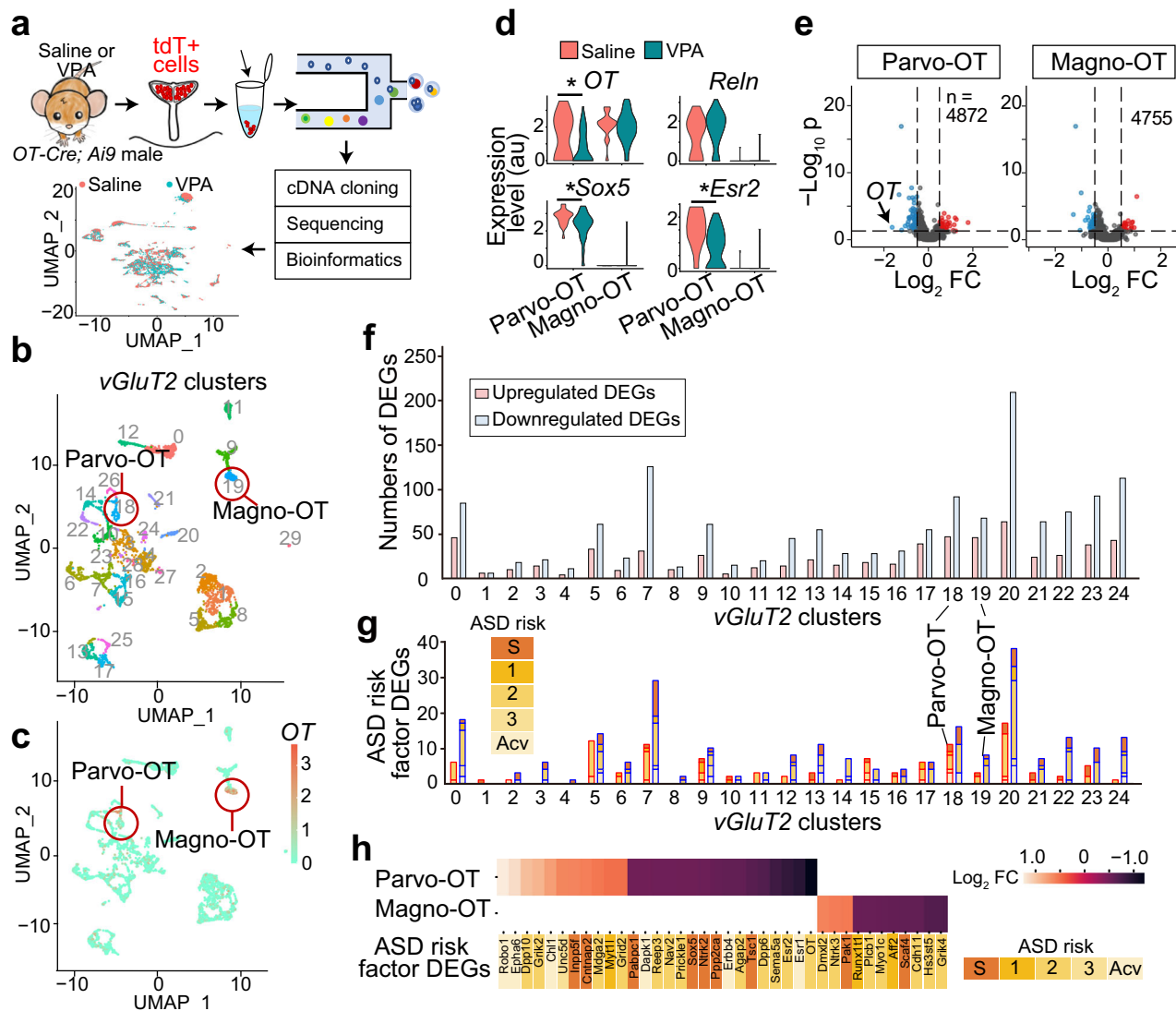
Fig. 2 | Transcriptomic profiles of PVH^OT neurons in VPA-treated mice.
a Schematics of single nucleus RNA-seq data collection and analysis. tdT, tdTomato from the Ai9 allele. Universal manifold approximation and projection (UMAP) representation of all nucleus data are also shown. **b,c** UMAP representation of vGluT2+ excitatory clusters (**b**) and OT gene expression, with a color scale showing log-normalized expression (**c**). **d** Violin plots of OT, and three genetic markers (Sox5, Reln, and Esr2 genes) to distinguish parvocellular (cluster 18) and magnocellular (cluster 19) PVH^OT neurons. *p < 0.05 by the two-sided Wilcoxon rank-sum test. **e** Volcano plots representing DEGs (upregulated, red dots; downregulated, blue dots) in the parvocellular and magnocellular PVH^OT neurons. The X-axis represents the log_2-transformed fold-change ratios, and the Y-axis represents the log_10-transformed p-value. The number (n) of genes analyzed is indicated in the panel. The p-values are based on the Wilcoxon Rank Sum test without adjustments for multiple comparisons. **f** The numbers of upregulated (red) and downregulated (blue) DEGs within the vGluT2+ clusters. Clusters 25–29 were excluded from the analysis as the number of nuclei was too small (fewer than 57). **g** Number of ASD risk factor DEGs within the upregulated (red frame) and downregulated (blue frame) DEGs. **h** Heatmaps of the log_2-transformed fold change for ASD risk factor DEGs found within the parvocellular and magnocellular PVH^OT neurons. The color codes for graphs (**g**) and gene names (**h**) show the rank of ASD risk[21]. For more data, see Supplementary Figs. 2–4. See Supplementary Information for exact p-values. Source data are provided as Source Data files.

---

were observed in VPA-treated mice expressing only hM3Dq without CNO, or expressing mCherry with CNO administration. However, administration of a single dose of CNO to hM3Dq-expressing VPA-treated mice restored their atypical social behaviors (Fig. 4b, right). Thus, chemogenetic activation of PVH^OT neurons ameliorated VPA-induced social dysfunctions.

Next, we generated hM3Dq-expressing VPA- or saline-treated mice, which received a single dose of CNO 1 week before the histochemical analysis to quantify OT ligand expression. In the saline-treated control group, the administration of CNO did not have a significant impact on the level of OT ligand expression (Fig. 4c, d). By contrast, CNO administration significantly restored the reduced expression of OT ligands in the FG− putative parvocellular PVH^OT

neurons in the VPA-treated group (Fig. 4c–e). To assess the time course of this recovery, we analyzed brain samples obtained 2.5 h, 1 day, 3 days, and 1 week after administering a single dose of CNO (Fig. 4f). We found that OT ligand expression in the FG− putative parvocellular PVH^OT neurons was unaltered at 2.5 h and 1 day after CNO administration. Subsequently, OT ligand expression gradually and significantly increased (Fig. 4g, h). These results demonstrate that a single chemogenetic neurostimulation of PVH^OT neurons during the adolescent stage is sufficient to provide a prolonged rescue of abnormal OT ligand expression in parvocellular PVH^OT neurons. Of note, we failed to establish a clear correlation between OT expression levels and behavioral performance, likely due to the limited quantitative precision of the three-chamber test (Supplementary Fig. 8a).
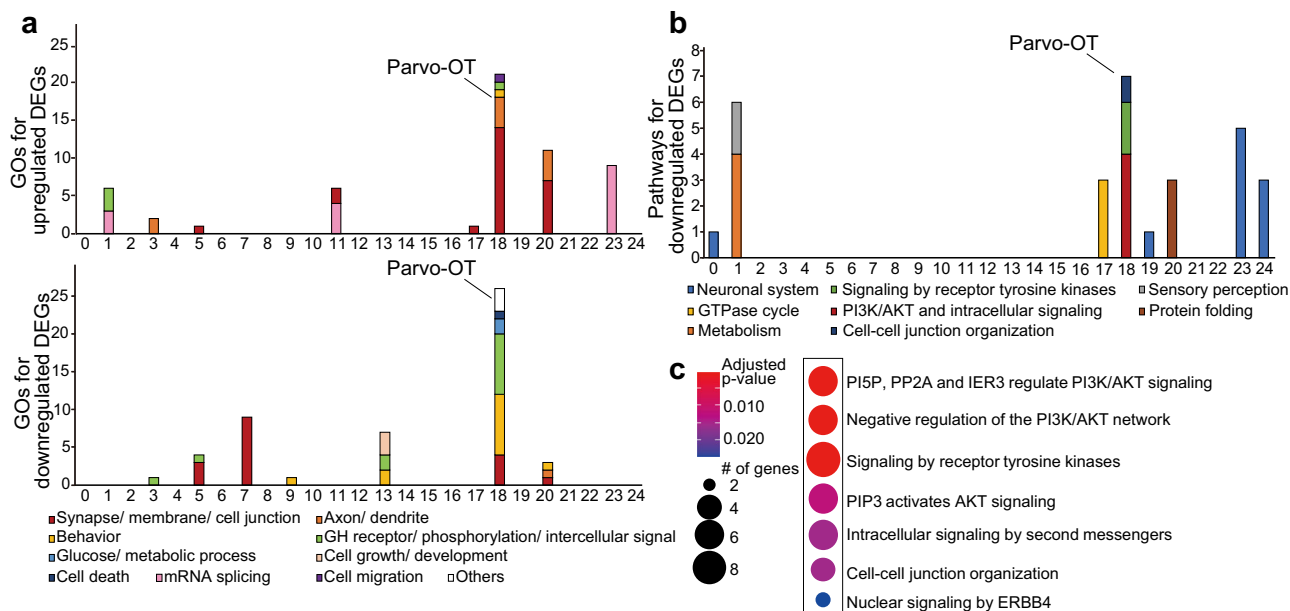
Fig. 3 | Gene Ontology (GO) and pathway analyses of DEGs. a,b The numbers of GO terms (**a**) and pathways (**b**) that show significant associations (GOs, $p < 0.01$ and pathways, $p < 0.05$) with DEGs within the top 25 *vGluT2*+ clusters. The full list of GO terms and pathways for each cluster is provided in Source Data files. The pathway analysis for the upregulated DEGs is shown in Supplementary Fig. 5c. **c** Heatmap of p-values for the pathway analysis using downregulated DEGs in the parvocellular PVH^{OT} neurons. The *p*-values are based on one-sided Fisher's exact test with Benjamini–Hochberg correction. For more data, see Supplementary Figs. 5–7. For abbreviations and details of the GO terms and pathways, see Source Data files.

To examine whether a single dose of CNO has a lasting positive impact on social behaviors and whether this treatment may also affect nonsocial behavioral abnormalities induced by prenatal VPA exposure[19], we next analyzed the behaviors of VPA-treated hM3Dq-expressing male mice at 1 week after CNO administration (Supplementary Fig. 8b). As a measure of nonsocial behaviors, we conducted the marble-burying test[40], which reflects repetitive, compulsive-like behaviors in mice. Consistent with previous findings[40], the VPA-treated group buried significantly more marbles than the saline-treated control group. However, these behaviors remained unaltered at 1.5 h after a single injection of CNO (Supplementary Fig. 8c). By sharp contrast, the results of the three-chamber test showed a significant improvement in sociability even 1 week after CNO administration (Supplementary Fig. 8d). Thus, a single dose of CNO does not reverse abnormal nonsocial behaviors while maintaining enduring positive effects on social behaviors. We also investigated whether optogenetic stimulation of PVH^{OT} neurons can restore OT ligand expression (Supplementary Fig. 9a). At 1 week following a 30-Hz, 1-hour optogenetic stimulation of PVH^{OT} neurons in VPA-treated male mice, we observed a significant increase in OT ligand expression within the putative parvocellular PVH^{OT} neurons in the posterior PVH (Supplementary Fig. 9b, c). These data suggest that high-frequency stimulation is sufficient for the recovery of OT expression.

Considering the prolonged effect observed, we hypothesized that the chemogenetic stimulation of OT neurons during the neonatal stage could potentially serve as a model of early intervention in atypical social behaviors. To investigate the consequence of prenatal VPA exposure during the neonatal stage, we examined sections of the PVH from *OT-Cre*; *Ai9* double heterozygous male mice at postnatal day (PND) 2. We observed comparable numbers of tdTomato-positive cells in both saline- and VPA-treated mice, indicating the presence of Cre-mediated recombination in the PVH^{OT} neurons during the neonatal stage (Fig. 5a–c). In contrast to the data at 5 weeks of age (Fig. 1), the number of OT ligand-expressing cells was unaltered in the VPA-treated group across the entire anterior–posterior axis of the PVH at PND 2

(Fig. 5a, b, d), suggesting that the reduction of OT expression in the parvocellular PVH^{OT} neurons occurs after PND 2.

To investigate the effects of the chemogenetic activation of OT neurons at PND 2, we generated double heterozygous male mice by crossing *OT-Cre* mice with a mouse line that drives hM3Dq-mCherry in a Cre-dependent manner[41]. These mice were subjected to embryonic VPA treatment and received a dose of CNO on PND 2 (Fig. 5e). We confirmed the specificity of hM3Dq expression in these mice through histochemical analysis (Supplementary Fig. 10). Subsequently, we evaluated their social behaviors using the three-chamber test at 5 weeks of age. We observed that the CNO-treated group displayed improved sociability compared with the saline-treated control group (Fig. 5f). Although neonatal CNO administration did not alter the number of hM3Dq-expressing PVH^{OT} neurons, OT ligand expression in hM3Dq-expressing posterior PVH^{OT} neurons was significantly restored compared with the saline-treated control group (Fig. 5g–k). These findings indicate that targeted neurostimulation of OT neurons during the neonatal stage ameliorates both the OT ligand expression and sociability of VPA-treated mice during later young adulthood, providing a valuable model for early intervention in the atypical development of social behaviors.

Transcriptomic analysis of PVH^{OT} neurons following chemogenetic stimulation

Next, we aimed to investigate the effects of neonatal OT neuron stimulation on gene expression in the PVH. We conducted snRNA-seq at 5 weeks of age using male *OT-Cre*; *stop-hM3Dq* mice that had been exposed to VPA prenatally and treated with either CNO or saline as a control at PND 2 (Fig. 6a). We obtained snRNA-seq profiles for 4635 and 4245 cells in the CNO- and saline-treated groups, respectively. Based on marker gene expression, we classified *vGluT2*+ clusters into one of the previously identified cell clusters based on Fig. 2b data (Fig. 6b, red, Supplementary Fig. 11a–d) and identified parvocellular and magnocellular PVH^{OT} neurons (Fig. 6c).
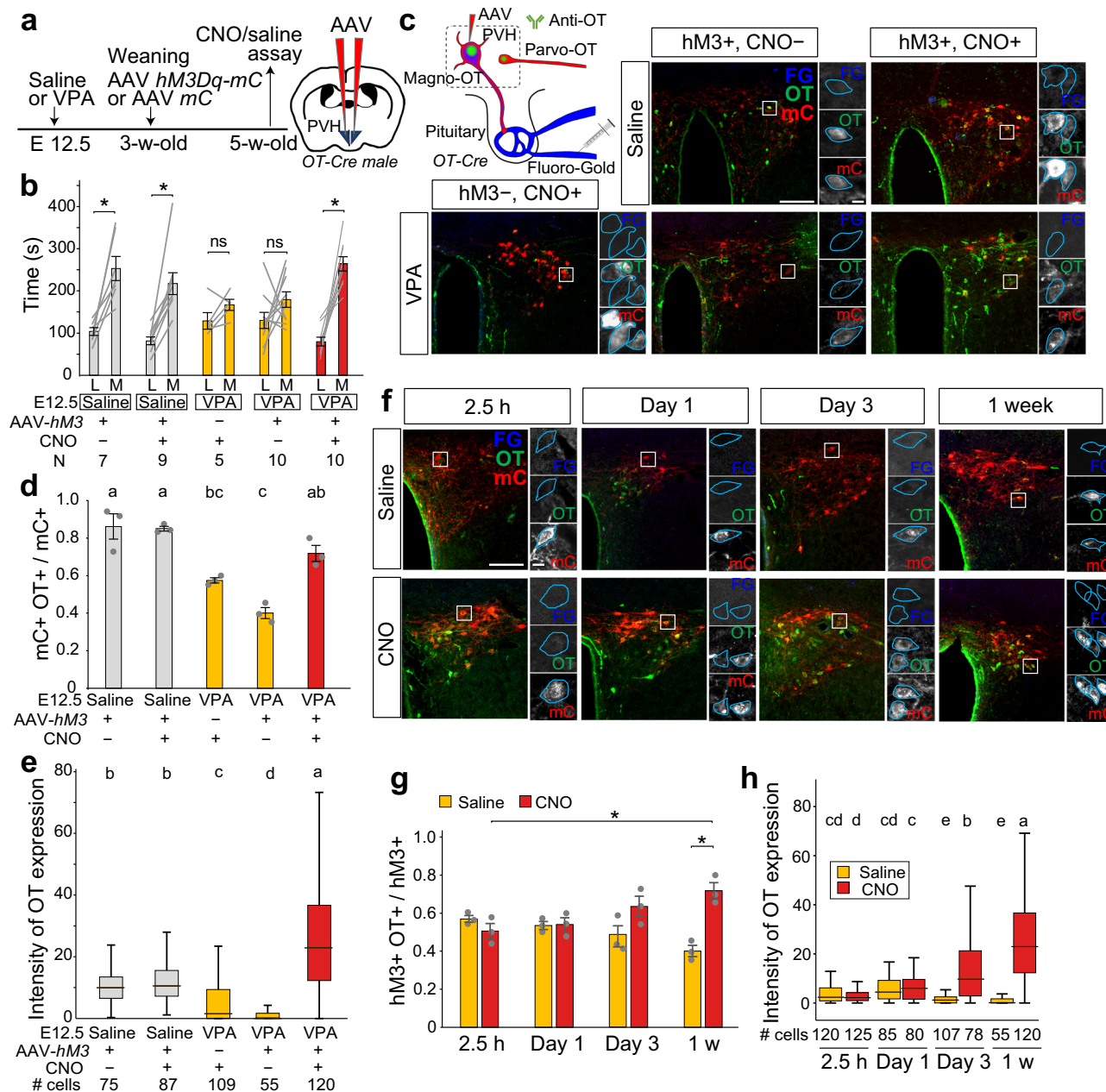
Fig. 4 | Chemogenetic activation of PVH^OT neurons rescues OT expression and atypical sociability. a Experimental time line and schematic of viral injection. mC, mCherry from AAVs. **b** Duration of mice exploring a Lego block (L) and an unfamiliar male mouse (M). The number of animals (N) is indicated in the panel. *$p < 0.05$ by the two-sided Wilcoxon rank-sum test with Bonferroni correction. **c** Typical coronal sections containing parvocellular PVH^OT neurons (FG−) in the posterior parts of the PVH showing mCherry (hM3Dq or control) and anti-OT staining (OT+). **d,e** Fraction of hM3Dq-mCherry+ OT+ cells over hM3Dq-mCherry+ cells (**d**) (N = 3 mice each) and fluorescent intensity of anti-OT staining in individual parvocellular PVH^OT neurons (**e**). The indicated number of cells were counted, from N = 3 animals each. Different letters (a–d) in the upper part of the graphs denote significant differences at $p < 0.05$ by one-way repeated measures ANOVA followed by the Tukey–Kramer post-hoc test (**d**) and one-way ANOVA with a post-hoc t-test with Bonferroni correction (**e**). **f** Time course analysis of the fraction of hM3Dq-

mCherry+ OT+ cells over hM3Dq-mCherry+ cells. **g** Time course analyses of the fraction of hM3Dq-mCherry+ OT+ cells over hM3Dq-mCherry+ cells. *$p < 0.05$ by the two-sided Wilcoxon rank-sum test. N = 3 mice each. **h** Fluorescent intensity of anti-OT staining in individual parvocellular PVH^OT neurons. The indicated number of cells were counted, from N = 3 animals each. Different letters (a–e) in the upper part of the graph denote significant differences at $p < 0.05$ by two-way ANOVA with a post-hoc t-test with Bonferroni correction. Scale bars, 200 μm for low-magnification images and 20 μm for magnified images. In **e** and **h**, the horizontal line within the box denotes the median, the upper and lower sides of the box indicate the first and the third quartiles, and whiskers represent the maximum and minimum values within a distance that extends to 1.5 times the interquartile range. Error bars, SEM. For more data, see Supplementary Figs. 8 and 9. See Supplementary Information for exact p-values. Source data are provided as Source Data files.

The DEG analysis unveiled more abundant upregulated genes within the CNO-treated group, particularly in parvocellular PVH^OT neurons (Fig. 6d–f, and Source Data files). These DEGs showed minimal overlap between parvocellular and magnocellular PVH^OT neurons (Fig. 6g). Remarkably, the OT gene itself was significantly upregulated

in the parvocellular PVH^OT neurons of CNO-treated mice (Fig. 6d, e, g), indicating that the observed recovery in OT ligand expression (Fig. 5g–k) was a result of restored mRNA expression. Additionally, the downregulated DEGs in the parvocellular PVH^OT neurons of the VPA-treated group (Fig. 2) displayed a significant trend of increased
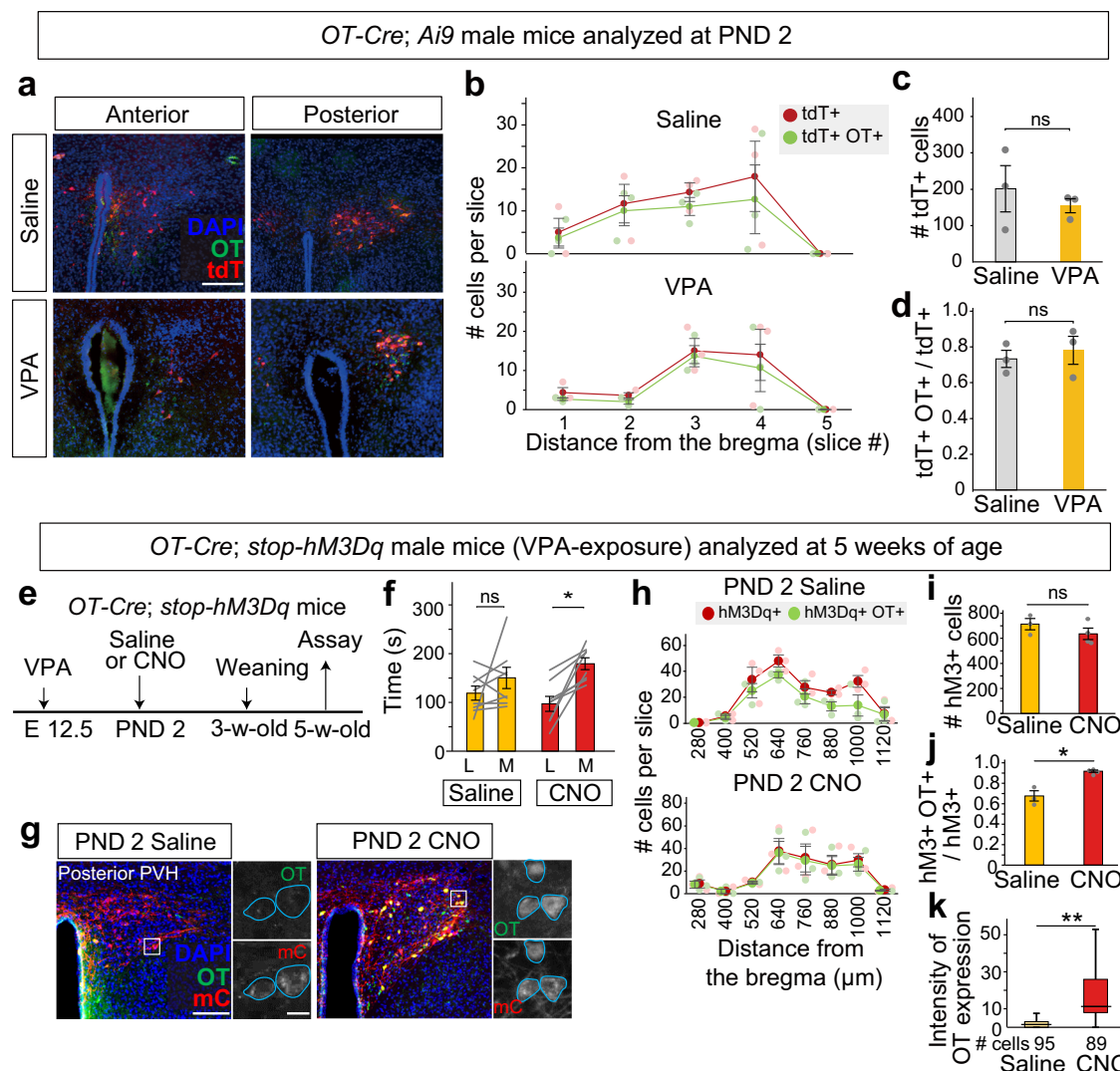
Fig. 5 | Neonatal activation of OT neurons persistently restores OT expression and social defects by VPA. a Typical coronal sections of the anterior and posterior parts of the PVH from *OT-Cre*; *Ai9* double heterozygous male mice at PND 2 that prenatally received either saline (top) or VPA (bottom) injection. Scale bar, 200 μm. PND, postnatal day. **b** Number of tdT+ cells and tdT+ OT+ dual-positive cells per slice along the anterior–posterior axis of the PVH. $N = 3$. **c** Number of tdT+ cells, which is not significantly different between the saline and VPA groups by the two-sided Wilcoxon rank-sum test ($N = 3$ mice). **d** Fraction of tdT+ OT+ cells over tdT+ cells. No difference was detected by the two-sided Wilcoxon rank-sum test ($N = 3$ mice). **e** Time line of the experiments. **f** Duration of mice exploring a Lego block (L) and an unfamiliar male mouse (M). $N = 8$ each for the saline and CNO groups. *$p < 0.05$ by the two-sided Wilcoxon rank-sum test. **g** Typical coronal sections of the posterior PVH showing mCherry (inference of hM3Dq) and anti-OT staining (OT +). Scale bars, 200 μm for low-magnification images and 20 μm for magnified images. **h** Number of hM3Dq-mCherry+ and hM3Dq-mCherry+ OT+ cells per slice along the

anterior–posterior axis of the PVH. $N = 3$ for the saline and $N = 4$ for the CNO group. **i** Number of hM3Dq-mCherry+ (hM3) cells. No significant difference was detected by the two-sided Wilcoxon rank-sum test. **j** The fraction of hM3Dq-mCherry+ OT+ cells over hM3Dq-mCherry+ cells. *$p < 0.05$ by the two-sided Wilcoxon rank-sum test. $N = 3$ for the saline and $N = 4$ for CNO groups (**i,j**). **k** Fluorescent intensity of anti-OT staining in individual cells, as in Fig. 1g in the posterior PVH, where parvocellular PVH^OT neurons exist. The horizontal line within the box denotes the median, the upper and lower sides of the box indicate the first and the third quartiles, and whiskers represent the maximum and minimum values within a distance that extends to 1.5 times the interquartile range. The indicated number of cells were counted, from $N = 3$ animals each. **$p < 0.01$ by the two-sided Wilcoxon rank-sum test. Error bars, SEM. For more data, see Supplementary Fig. 10. See Supplementary Information for exact p-values. Source data are provided as Source Data files.

expression in the CNO-treated group (Fig. 6h), indicating recovery. By contrast, the upregulated DEGs in the VPA group did not show a trend toward restoration. To validate gene expression recovery further, we visualized the expression of some of the upregulated DEGs found in parvocellular PVH^OT neurons in vivo through ISH. All four genes that we examined, including the *OT* gene, exhibited a significant increase in mRNA expression (Supplementary Fig. 12). The GO and pathway analyses of the upregulated DEGs highlighted enriched functionally relevant GO terms and pathways in parvocellular (Fig. 6i,j), but not magnocellular PVH^OT neurons (Supplementary Fig. 11e). Besides OT neurons, we observed a large number of upregulated DEGs in

other *vGluT2*+ clusters, including AVP-expressing (cluster 11) and thyrotropin-releasing hormone-expressing (cluster 12) neurons (Fig. 6f), suggesting the presence of non-cell autonomous effects of neonatal OT stimulation on other cell types in the PVH (Supplementary Fig. 11f). In contrast to *vGluT2*+ clusters, we found only a minimal effect on GABAergic neurons (Supplementary Fig. 11g, h).

In summary, these data demonstrate that neonatal OT neuron stimulation exerts a cell-type-specific and long-lasting positive influence on certain aberrant gene expressions in PVH neurons, including parvocellular PVH^OT neurons, which potentially contributes to the restoration of social behaviors.
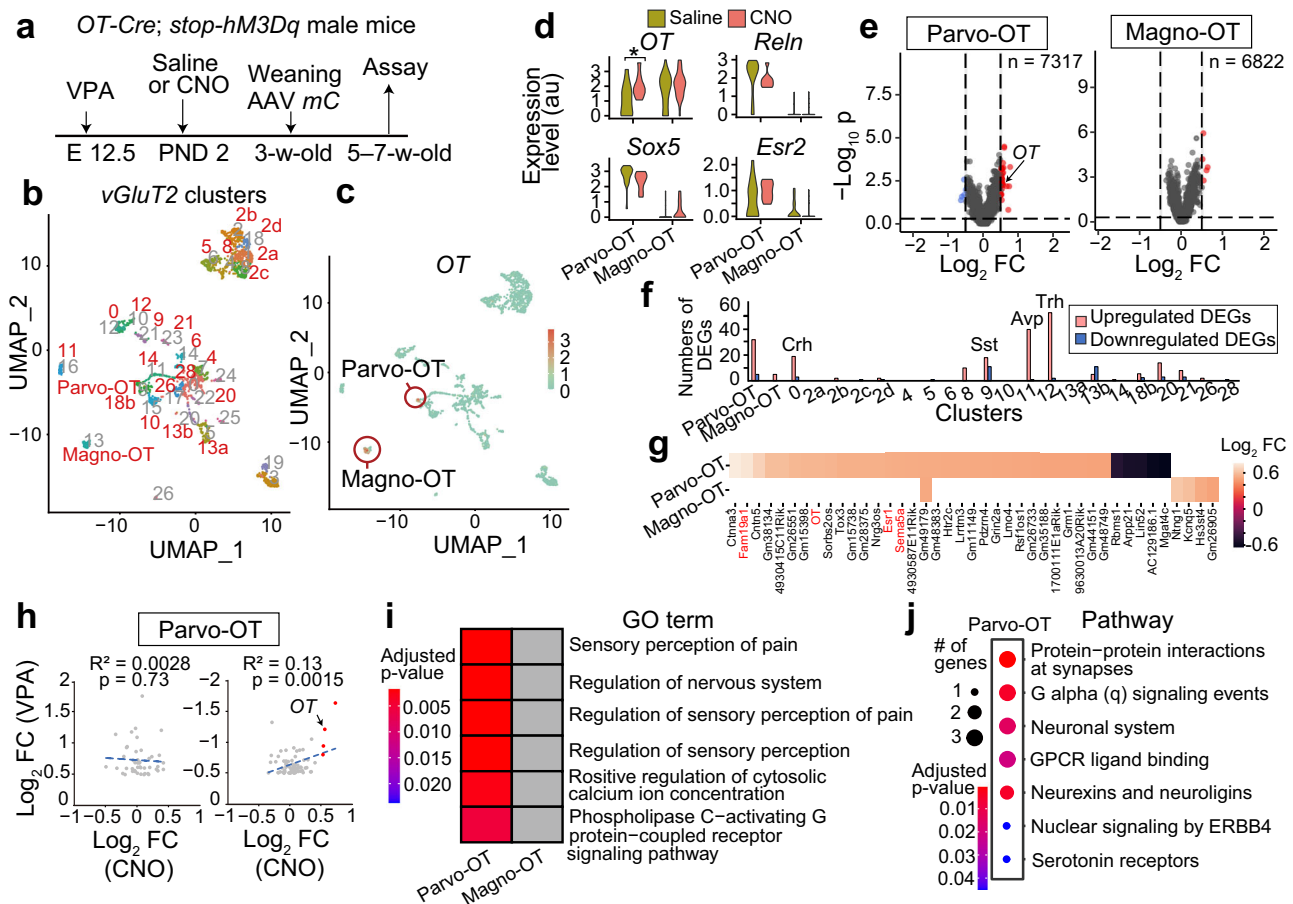
Fig. 6 | Long-lasting effects of neonatal stimulation of OT neurons. a Time line of the experiments. PND, postnatal day. **b,c** UMAP of *vGluT2*+ cell clusters (**b**) and *OT* gene expression (**c**), with a color scale showing log-normalized expression. The clusters highlighted in red correspond to the *vGluT2*+ clusters in Fig. 2b based on marker gene expressions (Supplementary Fig. 11b). **d** Violin plots showing *OT* gene expression, and three genetic markers (*Sox5*, *Reln*, and *Esr2* genes) used for distinguishing parvocellular and magnocellular PVH[OT] neurons. *$p < 0.05$ by the two-sided Wilcoxon rank-sum test. **e** Volcano plots representing upregulated (red) and downregulated (blue) DEGs in the parvocellular and magnocellular PVH[OT] neurons, as in Fig. 2e. The p-values are based on the Wilcoxon Rank Sum test without adjustments for multiple comparisons. **f** Numbers of upregulated (red) and downregulated (blue) DEGs within the *vGluT2*+ clusters (cluster names are based on Fig. 2b). **g** Heatmaps showing the log₂-transformed fold change for DEGs found in

the parvocellular and magnocellular PVH[OT] neurons. Genes downregulated in the VPA-treated group (Fig. 2e) are denoted in red. **h** Correlation between the log₂-transformed fold changes in the CNO-treated group (X-axis) and those in the VPA-treated group (Y-axis, left for upregulated and right for downregulated DEGs), based on Fig. 2 data. Red dots represent significantly upregulated genes in the CNO-treated group. The *p*-values are based on one-sided t-test. **i** GO terms associated with the upregulated DEGs are shown with a heatmap of p-values for each GO term in the parvocellular and magnocellular PVH[OT] neurons. Gray cells indicate no enrichment. **j** Heatmap representing p-values for pathway analysis using upregulated DEGs in the parvocellular PVH[OT] neurons. The *p*-values in **i** and **j** are based on one-sided Fisher's exact test with Benjamini−Hochberg correction. For more data, see Supplementary Figs. 11 and 12. See Supplementary Information for exact *p*-values. Source data are provided as Source Data files.

Discussion

Efforts to develop an effective treatment for atypical social traits in NDDs are impeded by our limited comprehension of the pathophysiology associated with the symptoms, particularly at the cellular level. Social dysfunction arises from a complex interplay between a multitude of genetic risk factors[42,43] and a wide range of maternal and environmental influences during fetal brain development[2,3], which have the potential to impact the entire nervous system. Previous research has predominantly centered on symptom-correlated traits in the cerebral cortex[44–46], whereas the hypothalamic regulators of social behavior have received comparatively little attention[5,12]. In the present study, we employed snRNA-seq to elucidate the specific effects on gene expression in the hypothalamic center regulating social behaviors, particularly focusing on social dysfunction and recovery models. Here, we discuss the biological insights yielded by our study, along with its limitations.

Although diminished OT immunoreactivity in the PVH is common in both genetic[5,16–18] and environmental[4,19,20] models of social

dysfunctions, previous research has not distinguished cellular loss from a reduction of OT expression. Our data have ruled out cellular depletion in PVH[OT] neurons in VPA-exposed mice. Instead, abnormalities in gene expression in parvocellular PVH[OT] neurons, including the *OT* gene, are particularly concentrated in vital neural functions and signal transductions. Consequently, the ability of parvocellular PVH[OT] neurons to convey information to downstream targets would be severely compromised. Analogous to the pronounced impacts on specific cell types seen in neurodegenerative disorders[1], the framework of selective vulnerability at the level of gene expression can facilitate our understanding of social dysfunctions in a broader context. Future studies utilizing transcriptome analysis should explore whether the reduction in *OT* expression is common in various genetic social dysfunction models[5,16–18], and whether it stems from a shared vulnerability in the gene regulatory system within parvocellular PVH[OT] neurons.

We have established that the chemogenetic stimulation of OT neurons exerts sustained effects on gene regulation in parvocellular

PVH[OT] neurons, correlating with restored sociability. What underlies these enduring effects? Given the absence of a decline in OT expression at the neonatal stage of VPA-treated mice (Fig. 5a–d), a plausible hypothesis is that prenatal factors such as VPA exposure could induce an epigenetic scar[19], subsequently disrupting the crucial gene regulatory network for social behavioral development beyond infancy. Neonatal chemogenetic activation could mitigate these epigenetic scars, resulting in enduring effects. Future studies should characterize the epigenetic status at various stages of social behavioral development. It is also interesting to consider the extent to which social interactions with the mother and littermates impact social behavioral development[47].

While intense optogenetic stimulation can restore OT expression in parvocellular PVH[OT] neurons, our data suggest that Gq-signaling through chemogenetic activation provides additional benefits to the recovery process (Supplementary Fig. 9). In this context, stimulating OT neurons with blood–brain barrier-permeable small molecular compounds may be of interest. Our snRNA-seq data suggest that signaling pathways involving estrogen receptor ERα/β, serotonin receptor 5-HTR2c, and PI3K/Akt could be potential targets for stimulating parvocellular PVH[OT] neurons (Figs. 3, 6 and Supplementary Fig. 4a). Collectively, our established model for early intervention, combined with snRNA-seq analysis, provides a valuable platform for investigating effective pharmaco-therapeutic strategies and underlying mechanisms, which may hold translational relevance.

Parvocellular PVH[OT] neurons can modulate diverse brain functions[11,15,44], including social reward[12,14,48]. Their local neural circuitry enables influence over magnocellular PVH[OT] neurons[49], thereby exerting control over the entire OT system and collectively regulating various circuit functions[10], such as the cortical excitatory/inhibitory balance[50,51]. Additionally, parvocellular PVH[OT] neurons impact gene expression across various cell types[32], including AVP neurons (Fig. 6), which also contributes to social behaviors[9]. Targeted genetic manipulations of parvocellular PVH[OT] neurons are crucial for dissecting their roles across diverse brain regions and cell types in regulating social behaviors. To achieve these goals in future investigations, utilizing a manipulation system based on the *OT* minipromoter[8,15], in conjunction with cell-type-specific marker genes identified in the present and a previous study[12], holds promise.

Finally, we acknowledge two major limitations of the present study. First, this research utilized male mice exclusively because of reported mixed effects on social behaviors in prenatally VPA-exposed female rodents[23,52]. Given the strong male bias in ASD[53] and the expression of various sex steroid-related genes by parvocellular PVH[OT] neurons (Figs. 2, 6, and Supplementary Fig. 5), further investigations into the potential sexually dimorphic effects of genetic and environmental perturbations on parvocellular PVH[OT] neurons are warranted. Second, we did not examine the activity patterns of PVH[OT] neurons associated with social behavior[14]. It would be particularly interesting to investigate the neural activity dynamics of parvocellular PVH[OT] neurons during social interaction in typically developed, VPA-exposed, or OT-mediated recovery model mice. To this end, single-cell resolution imaging techniques, such as microendoscopy[54], can be combined with the aforementioned genetic approach to target parvocellular PVH[OT] neurons.

Methods
Animals
All animal experiments were approved by the Institutional Animal Care and Use Committee of the RIKEN Kobe Branch (#A2017-15-13). *OT-Cre* mice (JAX #024234) were purchased from the Jackson Laboratory. *Rosa26[tm9(CAG-tdTomato)Hze]* mice (also known as *Ai9* mice) (JAX #007909) were kindly provided by Takeshi Imai, who purchased them from the Jackson Laboratory. *Rosa26[dreaddm3]* mice (also known as *stop-hM3Dq* mice) were kindly provided by Takeshi Sakurai. Wild-type C57BL/6J

female mice were purchased from Japan SLC, Inc. (Shizuoka, Japan) for crossing. All mice were maintained on a C57BL/6J background. Animals were housed at the animal facility of the RIKEN Center for Biosystems Dynamics Research (BDR) under ambient temperature (18–23 °C) and a 12-h light, 12-h dark cycle schedule. The humidity was maintained at approximately 45%. The mice were allowed free access to the laboratory diet (MFG; Oriental Yeast, Shiga, Japan; 3.57 kcal/g) and water unless otherwise mentioned. In the present study, we exclusively utilized male mice, as male biased impacts of prenatal VPA exposure on social behaviors have been previously documented[19,23].

VPA treatment
To generate a group of mice treated with VPA[19,22], we administrated sodium valproate (Sigma, #P4543) at a dosage of 500 mg/kg to pregnant female mice on gestation day 12.5, based on the identification of the mating day through the formation of a vaginal plug. For the control group of mice treated with saline, we injected 10 mL/kg saline to pregnant female mice at the same stage.

Behavioral assays
The three-chamber test was performed using an apparatus consisting of three chambers measuring 20 × 30 × 30 cm (width × length × height), with the two side rooms connected to the central room by a small 5 × 3 cm (width × height) passageway. The test was conducted according to previously described methods[55]. Briefly, the animals were allowed to habituate to the empty chamber for 10 min. Then, the grids were placed in both side chambers, and the animals were further allowed to habituate for 10 min. A non-familiar C57BL/6 young adult mouse or a Lego block was placed on the grid and the animal's behaviors were recorded for 10 min. The recording was done using a GoPro8 camera (GoPro; #CHDHX-801-FW). The experiment was conducted approximately around zeitgeber time (ZT) 6, where ZT 0 was defined at the onset of the light period. For pharmacogenetic activation during adolescence (Fig. 4), behavior sessions were initiated 30 min after intraperitoneal administration of CNO (5 mg/kg, Tocris, #4936/10) or saline (200 µL). For pharmacogenetic activation during the neonatal stage (Figs. 5, 6), CNO (5 mg/kg) or saline (10 µL) was orally administered on PND 2, and behavioral experiments were conducted at 5 weeks of age.

To evaluate social behaviors, we manually quantified the time spent by the mice exploring the grid containing the non-familiar mouse and the grid containing the object during the 10-min recording session. The investigation time was defined as the period during which the mice actively engaged in sniffing and exploring the grid. The side chambers were cleaned with ethanol between each habituation and recording session.

The marble-burying assay was conducted according to the protocols[40] in a 14 × 32 × 14 cm (width × length × height) cage with approximately 4 cm of wood chip bedding. The animals were allowed to habituate to the empty cage for 10 minutes. Twenty marbles were then placed in the cage and the animals' behaviors were recorded for 10 min. At the end of the test, the animals were removed from the cage and the buried marbles were manually counted. A marble was considered "buried" if two-thirds of its height was submerged in the bedding, as observed from a lateral view.

Single nucleus RNA sequencing (snRNA-seq): library preparation
The "Frankenstein" protocol (doi:10.17504/protocols.io.3fkgjkw) was modified to isolate the nucleus as follows. For Figs. 2 and 3 data, male *OT-Cre; Ai9* mice at 5 weeks of age were deeply anesthetized by isoflurane (Fujifilm, #099-06571), perfused by cold phosphate-buffered saline (PBS) to remove blood cells, and euthanized by decapitation. Brains were sectioned into 1000-µm coronal slices under microscopy and the sections were floated in 1% BSA-PBS (Nacalai Tesque, #0128197

and Takara, #T9181). The PVH was dissected based on the fluorescence of tdTomato in *OT-Cre; Ai9* male mice, and homogenized sufficiently in ice-cold Nuclei EZ Lysis Buffer (Millipore Sigma, N-3408). The resulting suspension was incubated on ice for 5 min and filtered through a 70-μm strainer. The nuclei were pelletized by centrifugation at $500 \times g$ and 4 °C for 5 min, and the supernatant was removed. The nuclei were resuspended in Nuclei EZ Lysis Buffer and pelletized again by centrifugation at 500×g and 4 °C for 5 min. They were then resuspended in 1% BSA-PBS containing 0.2 U/μL RNase Inhibitor (Roche, 3335399001) (Resuspension Buffer). We utilized 2–4 male mice for each condition, pooled the isolated nuclei, and centrifuged again at 500×g and 4 °C for 5 min to pellet the nuclei. The nuclei were then resuspended in resuspension buffer and 10 μg/mL DAPI, and filtered through a 40-μm strainer. The nuclei were sorted from the suspension using a cell sorter (SH800Z; Sony) at 5 °C. The gate was set first to identify a single nucleus population based on the DAPI signal and then to select larger nuclei preferentially, inferring neurons while simultaneously excluding multiplets (Supplementary Fig. 2a). Immediately after sorting was completed, the nuclei stained with DAPI were counted using a hemocytometer to verify the yield of intact nuclei. The nuclei were then resuspended in a resuspension buffer and used for generating snRNA libraries using the 10X Genomics Chromium platform targeting 8000 nuclei per condition. The libraries were prepared using the 10X Genomics RNA 3′ v3 kit (#1000269). The completed libraries were sequenced to a depth of 110 Gb on HiSeqX (performed by Novogene).

For Fig. 6 data, we utilized male *OT-Cre; stop-hM3Dq* mice at 5–7 weeks of age that had been exposed to VPA prenatally and CNO or saline as a control at PND 2. We followed the above protocols with slight modifications. Briefly, *OT-Cre; stop-hM3Dq* mice were injected with AAV in the PVH and the supraoptic nucleus regions at three weeks of age to facilitate visualization of OT neurons during the dissection process. To optimize the yield in collecting neural cell nuclei, the FACS gating was adjusted to accommodate larger nuclei. Each batch aimed to isolate 5000 nuclei using the Chromium system. The completed libraries were sequenced to a depth of 105 Gb on HiSeqX (performed by AZENTA).

snRNA-seq: data analysis

To conduct the analysis, we aligned the fastq files from each library to the mm10 reference transcriptome (mm10, gencode version vm23) using the Cell Ranger pipeline. After alignment, we loaded feature barcode matrices into Seurat (R package, v4.3.0). Cells were retained if at least 800 Unique Molecular Identifiers (UMIs) were detected, and genes were retained if at least one UMI was detected in at least three cells. In Figs. 2 and 3 data, after quality control and initial filtering, we recovered 5491 and 10,904 total nuclei from the saline and VPA libraries, respectively. The median numbers of genes/nuclei were 3232 for the saline library and 2460 for the VPA library. The saline library contained a considerable number of cells that appeared to be doublets, as evidenced by having more than twice the mean number of UMI and barcodes. To address this issue, we utilized Cloupe to confirm that a cell population containing 4300 or more barcodes formed a doublet cluster, and then removed such cells. Similarly, we removed cells with more than twice the mean number of UMI in the VPA library. The saline and VPA libraries were integrated using the sctransform function in Seurat. Normalization of the count data was conducted using LogNormalize. In this method, the following calculations were made. Feature counts for each cell were divided by the total counts for that cell and multiplied by the scale factor. This was then natural-log transformed using log1p.

We identified the top 3000 variable features and employed them as input for principal component analysis. We performed the initial clustering (Supplementary Fig. 2) using the top 35 principal components (PCs) at a resolution of 0.02 to distinguish between neuronal and non-neuronal cell populations. Based on the expression of *Camk2a*,

Slc17a6, *Gad1*, and *Gad2*, we identified the neuronal cell population and utilized the subsetUmapClust function to perform re-clustering. Furthermore, we separated the neuronal population into *vGluT2*+ and *Gad1/2*+ subpopulations based on the expression of *Slc17a6*, *Gad1*, and *Gad2* using the same parameters as before. We identified 1133 and 3225 nuclei in the saline and VPA libraries for the *vGluT2*+ neuronal population, respectively, which collectively constituted 30 clusters using the top 40 PCs at a resolution of 1.00. In Fig. 2a, b, we counted as follows. In the saline library, 17 and 21 nuclei were classified as magnocellular and parvocellular OT neurons, respectively, and in the VPA library, 94 and 90 nuclei were classified as magnocellular and parvocellular OT neurons, respectively. In Supplementary Fig. 7, we identified 17 clusters in the *GAD1/2* neuronal population using the top 40 PCs at a resolution of 0.25.

For Fig. 6 data, we followed the aforementioned procedures with minor adjustments. Briefly, we collected two batches, labeled as 1 and 2, for the CNO group, while data for the saline group were derived from a single batch. For both saline and CNO batch 1, we applied the method outlined above to eliminate nuclei forming doublets. Consequently, we removed nuclei with more than 5500 barcodes for saline and 5800 barcodes for CNO batch 1. Notably, in CNO batch 2, a considerable number of nuclei exhibited a trend of RNA degradation, as indicated by the Cell Ranger barcode rank plot. As a result, we focused our analysis on nuclei containing over 4000 barcodes based on the observation that parvocellular PVH^{OT} neurons found in saline and CNO batch 1 exhibited this range of barcodes per cell. We set the upper limit for barcodes in CNO batch 2 at 7000, considering that cells with barcodes approximately 1.8 times the lower limit could be singular. We performed the initial clustering using the top 50 PCs at a resolution of 0.02 to distinguish between neuronal and non-neuronal cell populations. Based on the expression of *Camk2a*, *Slc17a6*, *Gad1*, and *Gad2*, we identified the neuronal cell population and utilized the subsetUmapClust function to perform re-clustering using the top 30 PCs at a resolution of 0.50. In the saline and CNO libraries, we identified 880 and 1242 nuclei, respectively, within the vGluT2+ neuronal population, constituting a total of 27 clusters using the top 50 PCs at a resolution of 1.50.

In Supplementary Fig. 11, we identified magnocellular and parvocellular PVH^{OT} neurons in cluster 13 (corresponding to cluster 19 in Fig. 2) and cluster 9 (corresponding to cluster 18 in Fig. 2) within the *vGluT2*+ neuronal population using the top 20 PCs at a resolution of 0.9. In Fig. 6 and Supplementary Fig. 11, we counted as follows: In the saline library, 35 and 19 nuclei were classified as magnocellular and parvocellular OT neurons, respectively, while in the CNO library, 37 and 12 nuclei were classified as magnocellular and parvocellular OT neurons, respectively. The violin plots (Fig. 6d) for the CNO group were based on data from a representative batch.

Regarding the *GAD1/2*+ clusters in Supplementary Fig. 11, we limited our comparison to the saline and CNO batch 1, as CNO batch 2 had a lower number of barcodes. Utilizing the top 40 PCs at a resolution of 0.5, we identified 20 clusters and analyzed 1558 and 1348 nuclei in the saline and CNO libraries for the *GAD1/2*+ neuronal population, respectively.

snRNA-seq: DEGs, GO, and pathway analysis

We considered a gene to be "expressed" in a given cell type if at least one UMI was detected in 30% or more of the cells of that type. We then identified DEGs that exhibited upregulation or downregulation under the specific comparison conditions. DEGs were defined by an absolute $\log_2$-fold change ($|\log_2$-FC|) >0.5 and a *p*-value <0.05. A curated list of highly confident autism-associated genes was obtained from the SFARI Gene database (https://gene.sfari.org) as of 26 September 2023. In Fig. 2 and Source Data files, "SYNDROMIC", "CATEGORY 1", "CATEGORY 2", "CATEGORY 3" and "Archive only" genes in the SFARI Gene database were referred to as "S", "1", "2", "3", and "Acv", respectively.

In Figs. 3, 6, Supplementary Figs. 7, 11, and Source Data files, we conducted GO and pathway analyses of biological processes using clusterProfiler[28–30] for each cell cluster based on DEGs that were up- or down-regulated under the specified comparison conditions. The GO terms and pathways were sourced from an established compendium of designated terminologies. In cases where a single gene mapped to multiple isoform pathways, these were consolidated and treated as a singular pathway for the analysis.

Maternal high-fat diet (MHFD)
Female mice were housed with either a regular diet (RD) consisting of 5.5% of total kilocalories (kcal) from fat, 27.8% kcal from protein, and 48.6% kcal from carbohydrates (MFG; Oriental Yeast; 3.57 kcal/g), or a high-fat diet (HFD) consisting of 62.2% kcal from fat, 18.2% kcal from protein, and 19.6% kcal from carbohydrates (HFD-60; Oriental Yeast). After 8 weeks on the respective diets, female mice were mated with *OT-Cre* adult males. The HFD was continued throughout the pregnancy and lactation periods. The resultant offspring were weaned at 3 weeks of age and all were transitioned to the RD, regardless of their mothers' dietary condition.

Viral preparations
The following AAV vectors were generated by the Gunma University Viral Vector Core and Addgene using the corresponding plasmids. Titer of the viral vector is reported as genome particles (gp) per mL.

AAV serotype 8 *hSyn-DIO-hM3Dq-mCherry* (2.1×10^{13} gp/mL) (Addgene #44361)

AAV serotype 8 *hSyn-DIO-mCherry* (1.7×10^{13} gp/mL) (Addgene #50459)

AAV serotype 5 *EF1a-DIO-hChR2(H134R)-EYFP-WPRE-HGHpA* (1.8×10^{13} gp/mL) (Addgene #20298)

AAV serotype 5 *EF1a-DIO-EYFP* (1.6×10^{13} gp/mL) (Addgene #27056)

AAV serotype 9 *OTp-mCherry* (2.3×10^{13} gp/mL) (Addgene #184754)

Stereotactic and orbital venous plexus injections
Male mice (*OT-Cre, OT-Cre; Ai9*, and *OT-Cre; stop-hM3Dq*) at the age of 3 weeks were used for injection. All stereotaxic injections were performed under general ketamine–xylazine anesthesia, with 65 mg/kg ketamine (Daiichi-Sankyo) and 15 mg/kg xylazine (Sigma-Aldrich, cat# X1251), using a stereotaxic instrument (RWD, cat#68045). The coordinates for injection into the PVH were as follows: anterior 0.78 mm and lateral ± 0.1 mm from the bregma, and ventral 4.5 mm from the brain surface. 250 nL of either AAV8 *hSyn-DIO-hM3Dq-mCherry*, AAV8 *hSyn-DIO-mCherry*, AAV5 *EF1a-DIO-hChR2(H134R)-EYFP-WPRE-HGHpA*, or AAV5 *EF1a-DIO-EYFP* was bilaterally injected into the PVH at a speed of 50 nL/min using a UMP3 pump regulated by Micro-4 (World Precision Instruments). The coordinates for injection into the supraoptic nucleus were as follows: anterior 0.78 mm and lateral ± 0.2 mm from the bregma, and ventral 5.5 mm from the brain surface. 250 nL of either AAV serotype 9 *OTp-mCherry* was bilaterally injected into the PVH and the supraoptic nucleus at a speed of 50 nL/min using a UMP3 pump regulated by Micro-4 (World Precision Instruments).

To achieve selective labeling of magnocellular PVH[OT] neurons with FG, 30 μL of 2% FG (Fluorochrome, cat#526-94003) in saline was administered either unilaterally or bilaterally into the orbital venous plexus using a 1-mL syringe and 25-G needle. Animals were sacrificed for histochemical analysis at least 24 h after FG injection.

Optogenetic stimulation of PVH[OT] neurons
To activate PVH[OT] neurons using ChR2 (Supplementary Fig. 9), we followed protocols from previous studies[50,51]. Briefly, two weeks after AAV [AAV5 *EF1a-DIO-hChR2(H134R)-EYFP-WPRE-HGHpA* or AAV5 *EF1a-DIO-EYFP*] administration, an optical fiber (NA = 0.50, core diameter = 400 μm, Kyocera) was implanted bilaterally above the PVN (4.5 mm ventral from the brain surface). The implanted fiber was fixed on the skull with dental cement. After a one-week recovery period, the neurons were illuminated with a 465 nm blue laser light (IOS-465, RWD) at a frequency of 30 Hz, with a pulse width of 10 ms, for a duration of 1 h. The laser output intensity at the optical fiber tip was 4–6 mW/mm². Seven days later, brain tissue was collected for histochemical analysis.

Histology and histochemistry
Brains from *OT-Cre, OT-Cre; Ai9*, and *OT-Cre; stop-hM3Dq* mice were subjected to immunolabeling. The mice were anesthetized with an overdose of isoflurane and then perfused transcardially with PBS, followed by 4% paraformaldehyde (PFA) in PBS. Brain tissues were post-fixed overnight with 4% PFA in PBS at 4 °C, cryoprotected with 30% sucrose solution in PBS for at least 24 h, and embedded in O.C.T. compound (Tissue-Tek, cat#4583). We collected 30-μm coronal sections of the whole brain using a cryostat (model #CM1860; Leica) and placed them on MAS-coated glass slides (Matsunami, cat#MAS-13). The following primary antisera were used for immunolabeling: rabbit anti-OT (1:500, IMMUNOSTAR, cat#20068) and goat anti-mCherry (1:500, Acris Antibodies GmbH, cat# ACR-AB0040-200-0.6). The primary antisera were detected with the following secondary antibodies: donkey anti-rabbit Alexa Fluor 488 (1:250, Invitrogen, cat# A32790), donkey anti-goat Alexa Fluor 555 (1:500, Invitrogen, cat# A32816), and donkey anti-rabbit Alexa Fluor 647 (1:250, Invitrogen, cat#A31573). Sections were counterstained with DAPI (2.5 μg/mL) and imaged using an Olympus BX53 microscope equipped with a 10 × objective lens (numerical aperture 0.4).

In situ hybridization (ISH)
Fluorescent ISH was performed as previously described[56]. In brief, mice were deeply anesthetized with isoflurane and perfused with PBS, followed by 4% PFA in PBS. The brain was post-fixed with 4% PFA overnight. 30-μm coronal brain sections were made using a cryostat (Leica). To generate cRNA probes, DNA templates were amplified by PCR from the C57BL/6j mouse genome or whole-brain cDNA (Genostaff, cat#MD-01). T3 RNA polymerase recognition site (5′-AAT-TAACCCTCACTAAAGGG) was added to the 3′ end of the reverse primers. Primer sets to generate DNA templates for cRNA probes are as follows (the first one, forward primer, the second one, reverse primer):

Esr2–1 5′- AGACAAGAACCGGCGTAAAA; 5′- CGTGTGAGCATTCAG CATCT

Esr2–2 5′- CTCAATCTCGGGGTCTGAGT; 5′- CCAAGCAGGAAGAAA GAGGA

Tsc1–1 5′- AGGGGTTGCCTCACCTTACT; 5′- GGCACAGTCCTCCAA CCTTA

Tsc1–2 5′- GGGTGGAGGCTTCTGTTTTA; 5′- ACCAGGGTGTCCTGT GTCTC

Tsc1–3 5′- CTCAGTTTGCACTGCAGCAT; 5′- TGGCATCTGATTTGG ATTGT

Sox5–1 5′- CCCTCCATGTGGGAATAGAA; 5′- CAAACTTGAGGGTGG CATTT

Sox5–2 5′- AACGCATACAATGTGAAAACAGA; 5′- GGGCTTTAACC CATTTTCTTC

Sema5a–1 5′- CCCAACAAATCAAGCCAAAT; 5′- ATTTGCACCAGGC TCTGAAT

Sema5a–2 5′- CTCCACCCCTTCATAATCCA; 5′- TGGTGCATCTTAT TGGCAGA

Sema5a–3 5′- TGACTTGACACCTGCTACGC; 5′- TGTTTCTTAAATG GCAGGGTTT

Prickle1–1 5′- GAGGACCGCAGCTCTCAAC; 5′- ACCGAGGCTTGA GCAGTTC

Prickle1–2 5′- CGCTAACGAGGAATTCTGGA; 5′- AGTCTGTCCTTG GCGGAGTA

Prickle1–3 5′- GACTCGTGGTGTTCGTCCTC; 5′- ACAAGCAGTCACC TCATCCA

Ntrk2–1 5′- GACTGAGCCTGGAGATTTGC; 5′- CAAACCTGGAATGG AATGCT

Ntrk2–2 5′- TGCACACATGTAGTGTGTTTGTG; 5′- AGTGATGAATC CCTCCCAAC

Ntrk2–3 5′- ATTTTGCAGCCTACGCATTC; 5′- AGGGTGAGAGAA GCTGGTCA

Erbb4–1 5′- TGATGAGGACAATGACAAATGA; 5′- AGCATTCCAAA GGTGCTGAC

Erbb4–2 5′- TGGGGCAAATAGGAAATTGT; 5′- GCATTTGAAGGCA AAGGCTA

Erbb4–3 5′- CCTCCTGTGACTTTTGTTGGA; 5′- GTGCATGTGCCA TGAATGAT

OT 5′-TGGCTTACTGGCTCTGACCT; 5′- AGGAAGCGCGCTAAAGG TAT

Esr1–1 5′- TAAGAAGAATAGCCCTGCCTTG; 5′- ACAGTGTACGCAG GAGACAGAA

Esr1–2 5′- AGGCATGGTGGAGATCTTTG; 5′- AAGCCATGAGAT CGCTTTGT

Fam19a1–1 5′- GCATTCATTTGGGGATTCAC; 5′- GCCAGAACGAGT TTCAGAGG

Fam19a1–2 5′- GCTACTGAATGCCTGGGAAA; 5′- AAGAGATCCACT TGGCTTGC

Fam19a1–3 5′- TGTGAGGTGGCTGGTGTATC; 5′- TCAGAGTGACCC ACATGGAA

Htr2c–1 5′- GGTGCACCAGGCTTAATGAT; 5′- GAGACAGGGGCAT GACAAGT

Htr2c –2 5′- ATGCACATGACTGTGGTGGT; 5′- AGCAGGTCCACGA ATGAAAC

Htr2c –3 5′- CAGCTACTTGCACACCTTGG; 5′- GCAGTCTGTTGCA CGTGTCT

DNA templates (500–1000 ng) amplified by PCR were subjected to in vitro transcription with DIG (cat#11277073910) or Flu (cat#11685619910)-RNA labeling mix and T3 RNA polymerase (cat#11031163001) according to the manufacturer's instructions (Roche Applied Science). When possible, up to three independent RNA probes were mixed to increase the signal/noise ratio. For ISH combined with anti-mCherry staining, after hybridization and washing, sections were incubated with horseradish peroxidase-conjugated anti-Dig (Roche Applied Science cat#11207733910, 1:500) and goat anti-mCherry (1:500, Acris Antibodies GmbH, cat# ACR-AB0040-200-0.6) antibodies overnight. Signals were amplified by TSA-plus Biotin (AKOYA Bioscience, NEL749A001KT, 1:70 in 1 × plus amplification diluent) for 25 min, followed by washing, and then mCherry-positive cells were visualized by donkey anti-goat Alexa Fluor 555 (1:500, Invitrogen, cat# A32816).

Quantification and statistics: snRNA-seq data

All statistical analyses for sequencing data were performed in RStudio and R. VPA data were performed in RStudio Server v1.4.1717 and R v2.1.2. CNO data were performed in RStudio Server 2023.06.1 Build 524 and R v4.3.1. GO term and pathway analyses were performed in RStudio 2022.12.0 + 353 and R v4.2.2. Statistical tests and criteria used for snRNA-seq analyses are described in the relevant method details sections. The number of biological replicates for each experiment is stated in the relevant figure legends.

Quantification and statistics: histochemistry and ISH data

All image analysis was performed using napari software (doi:10.5281/zenodo.3555620, napari version 0.4.15, Python version 3.8.0, and Numpy version 1.23.1). To assess the intensity of anti-OT immunostaining and RNA probes in individual parvocellular PVH[OT] neurons, we selected coronal sections located posteriorly at 1000–1120 μm from the bregma, guided by Fig. 1f data indicating the near-zero presence of

FG+ tdT+ (magnocellular PVH[OT] neurons) in these regions. Similarly, for magnocellular PVH[OT] neurons, we opted for coronal sections located posteriorly at 520–640 μm from the bregma, where nearly all tdT+ cells were FG+. By utilizing the labels tool in napari, all tdTomato- or hM3Dq-mCherry- or YFP-positive cells present within these sections were selected as regions of interest (ROIs), and the fluorescence intensity at each ROI was calculated using napari-skimage-regionprops (version 0.5.3). We randomly collected 55–300 ROIs for OT+ cells from at least three animals for each condition. Finally, the background fluorescence intensity was subtracted, and statistical analysis was conducted utilizing the corrected fluorescent intensity. Of note, the scales in Fig. 1g and Supplementary Fig. 1g are different as the secondary antibodies used to detect anti-OT were different in these experiments because of a technical issue. Similarly, the scales in Fig. 4h and Supplementary Fig. 9c are different.

Statistics

Statistical tests were performed using Excel, Python, R, and js-STAR (version 1.6.0). All tests were two-tailed unless otherwise mentioned. No statistical method was used to determine the sample size. Sample sizes are similar to those used in the research field. The sample size and statistical tests used are indicated in the figure legends and Supplementary Table 1. Statistical significance was set at $p < 0.05$ unless otherwise mentioned. Mean ± standard error of the mean (SEM) was used to report statistics unless otherwise indicated. In the box-and-whisker plots, the horizontal line within the box denotes the median, while the upper and lower sides of the box symbolize the first quartile and the third quartile, respectively. Two whiskers from the upper and lower edges, respectively, encompass the maximum and minimum values within a distance that extends to 1.5 times the interquartile range. Any outliers beyond this range are excluded from the plot. In the experiments shown in Figs. 1, 4, 5 and Supplementary Figs. 1, 4, 6, 8, 9, and 12, experiments were conducted and analyzed by an experimenter who was blind to the experimental conditions.

Reporting summary

Further information on research design is available in the Nature Portfolio Reporting Summary linked to this article.

Data availability

The snRNaseq data generated in this study have been deposited in the Gene Expression Omnibus database under accession code GSE245555. Source data are provided with this paper.

Code availability

This paper does not report the original code. All Python and R scripts used in this manuscript are provided with this paper.

References

1. Fu, H., Hardy, J. & Duff, K. E. Selective vulnerability in neurodegenerative diseases. *Nat. Neurosci.* **21**, 1350–1358 (2018).
2. Han, V. X., Patel, S., Jones, H. F. & Dale, R. C. Maternal immune activation and neuroinflammation in human neurodevelopmental disorders. *Nat. Rev. Neurol.* **17**, 564–579 (2021).
3. Kwon, H. K., Choi, G. B. & Huh, J. R. Maternal inflammation and its ramifications on fetal neurodevelopment. *Trends Immunol.* **43**, 230–244 (2022).
4. Buffington, S. A. et al. Microbial reconstitution reverses maternal diet-induced social and synaptic deficits in offspring. *Cell* **165**, 1762–1775 (2016).
5. Sgritta, M. et al. Mechanisms underlying microbial-mediated changes in social behavior in mouse models of autism spectrum disorder. *Neuron* **101**, 246–259.e246 (2019).
6. Froemke, R. C. & Young, L. J. Oxytocin, neural plasticity, and social behavior. *Annu. Rev. Neurosci.* **44**, 359–381 (2021).

7. Chen, P. & Hong, W. Neural circuit mechanisms of social behavior. *Neuron* **98**, 16–30 (2018).

8. Inada, K. et al. Plasticity of neural connections underlying oxytocin-mediated parental behaviors of male mice. *Neuron* **110**, 2009–2023 (2022).

9. Lukas, M. & Neumann, I. D. Oxytocin and vasopressin in rodent behaviors related to social dysfunctions in autism spectrum disorders. *Behav. Brain Res* **251**, 85–94 (2013).

10. Newmaster, K. T. et al. Quantitative cellular-resolution map of the oxytocin receptor in postnatally developing mouse brains. *Nat. Commun.* **11**, 1885 (2020).

11. Althammer F, Grinevich V. Diversity of oxytocin neurons: beyond magno- and parvocellular cell types? *J Neuroendocrinol*, https://doi.org/10.1111/jne.12549 (2017).

12. Lewis, E. M. et al. Parallel social information processing circuits are differentially impacted in autism. *Neuron* **108**, 659–675.e656 (2020).

13. Xiao, L., Priest, M. F., Nasenbeny, J., Lu, T. & Kozorovitskiy, Y. Biased oxytocinergic modulation of midbrain dopamine systems. *Neuron* **95**, 368–384.e365 (2017).

14. Hung, L. W. et al. Gating of social reward by oxytocin in the ventral tegmental area. *Science* **357**, 1406–1411 (2017).

15. Knobloch, H. S. et al. Evoked axonal oxytocin release in the central amygdala attenuates fear response. *Neuron* **73**, 553–566 (2012).

16. Resendez, S. L. et al. Social stimuli induce activation of oxytocin neurons within the paraventricular nucleus of the hypothalamus to promote social behavior in male mice. *J. Neurosci.* **40**, 2282–2295 (2020).

17. Dombret, C. et al. Loss of Maged1 results in obesity, deficits of social interactions, impaired sexual behavior and severe alteration of mature oxytocin production in the hypothalamus. *Hum. Mol. Genet* **21**, 4703–4717 (2012).

18. Muscatelli, F. et al. Disruption of the mouse Necdin gene results in hypothalamic and behavioral alterations reminiscent of the human Prader-Willi syndrome. *Hum. Mol. Genet* **9**, 3101–3110 (2000).

19. Nicolini, C. & Fahnestock, M. The valproic acid-induced rodent model of autism. *Exp. Neurol.* **299**, 217–227 (2018).

20. Dai, Y. C. et al. Neonatal oxytocin treatment ameliorates autistic-like behaviors and oxytocin deficiency in valproic acid-induced rat model of autism. *Front Cell Neurosci.* **12**, 355 (2018).

21. Abrahams, B. S. et al. SFARI Gene 2.0: a community-driven knowledgebase for the autism spectrum disorders (ASDs). *Mol. Autism* **4**, 36 (2013).

22. Kataoka, S. et al. Autism-like behaviours with transient histone hyperacetylation in mice treated prenatally with valproic acid. *Int J. Neuropsychopharmacol.* **16**, 91–103 (2013).

23. Kim, K. C. et al. Male-specific alteration in excitatory post-synaptic development and social interaction in pre-natal valproic acid exposure model of autism spectrum disorder. *J. Neurochem* **124**, 832–843 (2013).

24. Wu, Z. et al. An obligate role of oxytocin neurons in diet induced energy expenditure. *PLoS One* **7**, e45167 (2012).

25. Madisen, L. et al. A robust and high-throughput Cre reporting and characterization system for the whole mouse brain. *Nat. Neurosci.* **13**, 133–140 (2010).

26. Zheng, G. X. et al. Massively parallel digital transcriptional profiling of single cells. *Nat. Commun.* **8**, 14049 (2017).

27. Hao, Y. et al. Integrated analysis of multimodal single-cell data. *Cell* **184**, 3573–3587.e3529 (2021).

28. Yu, G., Wang, L. G., Yan, G. R. & He, Q. Y. DOSE: an R/Bioconductor package for disease ontology semantic and enrichment analysis. *Bioinformatics* **31**, 608–609 (2015).

29. Wu, T. et al. clusterProfiler 4.0: a universal enrichment tool for interpreting omics data. *Innov. (Camb.)* **2**, 100141 (2021).

30. Yu, G. & He, Q. Y. ReactomePA: an R/Bioconductor package for reactome pathway analysis and visualization. *Mol. Biosyst.* **12**, 477–479 (2016).

31. Sanchez-Alegria, K. Flores-Leon, M. Avila-Munoz, E. Rodriguez-Corona, N. & Arias, C. PI3K Signaling in Neurons: A Central Node for the Control of Multiple Functions. *Int J Mol Sci.* **19**, 3725 (2018).

32. Tyzio, R. et al. Oxytocin-mediated GABA inhibition during delivery attenuates autism pathogenesis in rodent offspring. *Science* **343**, 675–679 (2014).

33. Armbruster, B. N., Li, X., Pausch, M. H., Herlitze, S. & Roth, B. L. Evolving the lock to fit the key to create a family of G protein-coupled receptors potently activated by an inert ligand. *Proc. Natl Acad. Sci. USA* **104**, 5163–5168 (2007).

34. Grund, T. et al. Chemogenetic activation of oxytocin neurons: temporal dynamics, hormonal release, and behavioral consequences. *Psychoneuroendocrinology* **106**, 77–84 (2019).

35. Choe, K. Y. et al. Oxytocin normalizes altered circuit connectivity for social rescue of the Cntnap2 knockout mouse. *Neuron* **110**, 795–808.e796 (2022).

36. Penagarikano, O. et al. Exogenous and evoked oxytocin restores social behavior in the Cntnap2 mouse model of autism. *Sci. Transl. Med* **7**, 271ra278 (2015).

37. Harony-Nicolas, H. et al. Oxytocin improves behavioral and electrophysiological deficits in a novel Shank3-deficient rat. *Elife* **6**, e18904 (2017).

38. Teng, B. L. et al. Prosocial effects of oxytocin in two mouse models of autism spectrum disorders. *Neuropharmacology* **72**, 187–196 (2013).

39. Ino, D., Tanaka, Y., Hibino, H. & Nishiyama, M. A fluorescent sensor for real-time measurement of extracellular oxytocin dynamics in the brain. *Nat. Methods* **19**, 1286–1294 (2022).

40. Huang, F. et al. Betaine ameliorates prenatal valproic-acid-induced autism-like behavioral abnormalities in mice by promoting homocysteine metabolism. *Psychiatry Clin. Neurosci.* **73**, 317–322 (2019).

41. Takahashi, T. M. et al. A discrete neuronal circuit induces a hibernation-like state in rodents. *Nature* **583**, 109–114 (2020).

42. Bourgeron, T. From the genetic architecture to synaptic plasticity in autism spectrum disorder. *Nat. Rev. Neurosci.* **16**, 551–563 (2015).

43. Gaugler, T. et al. Most genetic risk for autism resides with common variation. *Nat. Genet* **46**, 881–885 (2014).

44. Nakai, N., Overton, E. T. N. & Takumi, T. Optogenetic approaches to understand the neural circuit mechanism of social deficits seen in autism spectrum disorders. *Adv. Exp. Med Biol.* **1293**, 523–533 (2021).

45. Gandal, M. J. et al. Broad transcriptomic dysregulation occurs across the cerebral cortex in ASD. *Nature* **611**, 532–539 (2022).

46. Del Pino, I., Rico, B. & Marin, O. Neural circuit dysfunction in mouse models of neurodevelopmental disorders. *Curr. Opin. Neurobiol.* **48**, 174–182 (2018).

47. Campolongo, M. et al. Sociability deficits after prenatal exposure to valproic acid are rescued by early social enrichment. *Mol. Autism* **9**, 36 (2018).

48. Dolen, G., Darvishzadeh, A., Huang, K. W. & Malenka, R. C. Social reward requires coordinated activity of nucleus accumbens oxytocin and serotonin. *Nature* **501**, 179–184 (2013).

49. Tang, Y. et al. Social touch promotes interfemale communication via activation of parvocellular oxytocin neurons. *Nat. Neurosci.* **23**, 1125–1137 (2020).

50. Marlin, B. J., Mitre, M., D'Amour, J. A., Chao, M. V. & Froemke, R. C. Oxytocin enables maternal behaviour by balancing cortical inhibition. *Nature* **520**, 499–504 (2015).

51. Froemke, R. C. & Carcea, I. Oxytocin and Brain Plasticity. *Principles of Gender-Specific Medicine*, 161–182 (2017).

52. Maisterrena, A. et al. Female mice prenatally exposed to valproic acid exhibit complex and prolonged social behavior deficits. *Prog. Neuropsychopharmacol. Biol. Psychiatry* **131**, 110948 (2024).

53. Fombonne, E. Epidemiological trends in rates of autism. *Mol. Psychiatry* **7**, S4–S6 (2002).
54. Ghosh, K. K. et al. Miniaturized integration of a fluorescence microscope. *Nat. Methods* **8**, 871–878 (2011).
55. Rein, B., Ma, K. & Yan, Z. A standardized social preference protocol for measuring social deficits in mouse models of autism. *Nat. Protoc.* **15**, 3464–3477 (2020).
56. Ishii, K. K. et al. A labeled-line neural circuit for pheromone-mediated sexual behaviors in mice. *Neuron* **95**, 123–137.e128 (2017).

Author contributions
M.T. and K.M. conceived the experiments. M.T. performed all the experiments and analyzed the data, with technical support from T.G., M.H., and S.I. M.T. and K.M. wrote the paper with help from all the authors.

Competing interests
The authors declare no competing interests.

Additional information
Supplementary information The online version contains supplementary material available at https://doi.org/10.1038/s41467-024-53092-w.

Correspondence and requests for materials should be addressed to Kazunari Miyamichi.

Peer review information *Nature Communications* thanks Dayu Lin, Takuya Osakada and the other, anonymous, reviewer for their contribution to the peer review of this work. A peer review file is available.

Reprints and permissions information is available at http://www.nature.com/reprints

Publisher's note Springer Nature remains neutral with regard to jurisdictional claims in published maps and institutional affiliations.